Geometrical-based algorithm for variational segmentation and smoothing of vector-valued images

S. Mahmoodi and B.S. Sharif

Abstract: An optimisation method based on a nonlinear functional is considered for segmentation and smoothing of vector-valued images. An edge-based approach is proposed to initially segment the image using geometrical properties such as metric tensor of the linearly smoothed image. The nonlinear functional is then minimised for each segmented region to yield the smoothed image. The functional is characterised with a unique solution in contrast with the Mumford–Shah functional for vector-valued images. An operator for edge detection is introduced as a result of this unique solution. This operator is analytically calculated and its detection performance and localisation are then compared with those of the *DroG* operator. The implementations are applied on colour images as examples of vector-valued images, and the results demonstrate robust performance in noisy environments.

1 Introduction

Vector-valued images such as colour, multi-spectral and multi-modal images can provide more valuable information than scalar images in applications ranging from satellite remote sensing to medical imaging. Vector-valued images can also be generated by extracting feature vectors from a single image as a part of image segmentation. In this paper, a variational method is considered for segmentation and smoothing of vector-valued images. Variational methods in image processing and computer vision are well established. The restoration known as 'inverse' problem was initially considered by Tikhonov and Arsenin [1] as an energy optimisation problem based on L_2 norm. The advantage of Tikhonov and Arsenin's method was that it was linear and easy to implement. Owing to its linearity, the smoothing was performed across discontinuities as well as every where else. Such a method therefore leads to blurred edges in restoration. This method was further modified by Rudin *et al.* [2] to introduce the notion of total variation based on L_1 norm in order to preserve edges when removing the noise. The minimisation of the functional proposed in the total variation method leads to a nonlinear differential equation whose solution was demonstrated in [2] to preserve discontinuities when it approaches to a low-pass image in regions where there are no discontinuities, hence removing the noise. This method was further generalised for vector-valued images in [3] and applied to RGB images as an example. The generalisation of the total variation method for noise removal in textures is still a challenge. In another development, Kass *et al.* [4] initially introduced a contour evolution method known as the 'snake' algorithm for image segmentation based on the optimisation of a linear functional in which three terms were minimised. The first and second terms were proportional to the first and second derivatives of an affinely parametrised contour. The third term was associated with the gradient of a given input image. One of the major drawbacks of the method proposed in [4] was that its implementation was not able automatically to adjust the topology of the evolving contour according to the topology of the objects in a given image. Another disadvantage of the method proposed in [4] was that it fell into local minima. Active balloons were then proposed in [5] to avoid local minima. The level set method proposed by the pioneering work of Sethian *et al.* (e.g. see [6–8]) introduced a mathematical solution to the problem of adjusting the evolving contour automatically according to objects' topologies by adding one dimension to the contour representation. Caselles *et al.* (e.g. see [6, 9–13]) employed the level set method to propose a variational contour evolution scheme for the image segmentation known as 'geodesic active contour' model for single- and vector-valued images. The proposed functional in geodesic active contour seeks the contours (solutions) whose length is minimised in a feature space produced by the gradient of a given input image. In such a feature space, considered as a Riemannian manifold, the contours with minimised length are the geodesics of the manifold. On the other hand, Mumford and Shah [14] proposed a nonlinear variational model for image segmentation and smoothing based on first variation calculations. Three terms are considered in the Mumford–Shah framework: (1) smoothing term causing the solution image to be as smooth as possible, (2) fidelity term causing the smoothed image to be as close as possible to the original image and (3) contour length minimisation term smoothing the contours which represent discontinuities and removing any unwanted contours. In this framework, the derivative operations are not performed across discontinuities resulting in nonlinearity. The implementation of this functional is difficult because of (i) the nonlinearity of this variational

doi:10.1049/iet-ipr:20060218

Paper first received 24th January 2006 and in revised form 15th January 2007

S. Mahmoodi is with the Psychology Division, School of Biology and Psychology, Henry Wellcome Building, Newcastle University, Framlington Place, Newcastle upon Tyne NE2 4HH, UK

B.S. Sharif is with the School of Electrical, Electronic and Computer Engineering, Merz Court, Newcastle University, Newcastle upon Tyne NE1 7RU, UK

E-mail: sasan.mahmoodi@ncl.ac.uk

framework, (ii) the fact that one of the solutions (smoothed image) of the functional is associated with the Banach space [15], whereas the other one (contour) is not associated with any known space and (iii) the fact that the solutions are represented with different dimensions, that is, the smoothed image is a two-dimensional manifold, whereas the contour is a one-dimensional manifold; both are in a three-dimensional Euclidean manifold. Different methods were therefore proposed to approximate and implement the Mumford–Shah functional (e.g. see [6, 9, 16–25]). These methods can be grouped into three major categories:

(a) Grayson–Gage–Hamilton-based approaches in which a contour is evolved under Mumford–Shah gradient flow [14]. The main advantage of this method is that if the evolving contour is far from any discontinuity, it evolves under its own curvature. Hence the algorithm does not fall into local minima. It is demonstrated (e.g. see [7]) that a curve moving under its own curvature shrinks to a point and also that it has smoothing effects on the contour in a neighbourhood of discontinuities. These important features are employed in this approach to implement the functional (e.g. [16]). One of the disadvantages of this approach is that small time steps are required to avoid any numerical instability [8]; hence the algorithm is slow to reach the convergence.
(b) Chan–Vese approach [17, 19–22] in which the minimisation is performed with respect to the signed distance function as well as to the variables in Mumford–Shah functional. One of the advantages of this approach is that it is numerically more stable and hence faster than algorithms in the first category. The main disadvantage is that it falls into local minima when the evolving contour is far from any discontinuity in the case of the piecewise continuous approximation of the functional.
(c) Ambrosio–Tortorelli-based approaches [23–25] in which a better behaved functional approaching the Mumford–Shah functional is proposed by using the Γ-convergence. The implementation methods in this approach do not employ any contour evolution scheme.

Mahmoodi *et al.* proposed a generic approach for signal and image segmentation and smoothing applicable to signals with any dimension, based on the second variation with respect to points and contours that represent discontinuities [26–29]. It was demonstrated that points or contours that represent discontinuities were minimisers of the functional proposed in [26–29]. A variational-based solution to the functional for piecewise continuous low-pass signals was proposed in [27]. An operator-based geometrical approach being faster and more robust in the presence of excessive noise was proposed in [28] to implement the functional introduced in [27]. This operator-based approach was generalised for grey-scale images based on the geometrical properties of surfaces (smoothed images) [26]. Implicit smoothing was employed to modify the functional introduced in [27] to segment and reconstruct piecewise continuous band-pass signals [29]. Differences between this proposed functional and the Mumford–Shah functional are as follows:

1. There is no unique solution for Mumford–Shah functional (e.g. see [19]), whereas the functional investigated in this study is characterised with a unique solution. Intuitively, the solutions for grey-scale and vector-valued images correspond to the edges (discontinuities) in an image. This is not the case in the Mumford–Shah functional because contours do not normally correspond to the edges (discontinuities) because of the smoothing property of the contour length minimisation term. Two numerical examples are presented in Section 4 to show this difference between the two functionals. The uniqueness of the solution means that the functional can be implemented using an operator as demonstrated in [26] for grey-scale images and is generalised in this paper for vector-valued images. However, it is possible to implement this functional using contour evolution schemes. In fact, this generic functional models the edge (discontinuity) detection process, hence the result of any edge detection algorithm can be considered as a solution of this functional.
2. The implementation of the functional considered in this paper is characterised with less mathematical and numerical complexity than that of the Mumford–Shah functional, mainly because the contour length minimisation is not performed in the investigated functional. The contour length minimisation term in the Mumford–Shah functional introduces

   (i) mathematical complexity so that the generalisation to 3D is a well-known challenge,
   (ii) numerical complexity and instability so that in a contour evolution scheme, one needs to employ a semi-implicit finite difference method to increase numerical stability [19] at the cost of increased numerical complexity. However, a perfect numerical stability is not yet achieved.

3. Unlike the investigated functional which is generic and can simply be modified for 1D signals as demonstrated in [27–29], the Mumford–Shah functional fails to model 1D signal segmentation and smoothing as the notion of contours is meaningless in a signal processing context [27, 29].

The importance of the investigated functional can be summarised as follows.

1. In contrast to Mumford–Shah functional, the investigated functional here unifies the processing of signals with any dimension, that is, a unique framework used in 1D signals can be applied to 2D, vector-valued and 3D volumetric images.
2. As inherited from Mumford–Shah functional, the segmentation and restoration are integrated by the investigated functional in this paper.
3. An operator-based method can be deduced from this variational framework.

One of the novelties of this paper is that the geometrical approach proposed in [28] for signals and in [26] for grey-scale images is generalised for vector-valued images. The generalisation of the variational framework presented in [26–29] for the vector-valued images demonstrates that this variational framework is generic and applicable to signals with any dimension. The uniqueness of the solution associated with the investigated functional enables us to propose an operator to find the solutions (edges) corresponding to discontinuities. It is important to understand the underlying operator employed for discontinuity detection for signals in [28], for grey-scale images in [26] and for vector-valued images in this paper. The derivation of this operator helps us to

1. compare the performance indices of this operator with those of other known operators,
2. understand how to improve the algorithms employing this operator and
3. understand how to derive new operators for the segmentation of more complicated images such as textures.

A mathematical analysis is therefore presented here to calculate the operator associated with this functional and its detection performance and localisation indices in comparison with a well-known operator such as *DroG*, which is the other original contribution of this work compared with previous ones.

The geometrical properties such as the discriminant of the metric tensor of the linearly smoothed images composing a hyper-surface are employed to detect discontinuities. Having segmented the image, the functional considered in this paper is then minimised to smooth the image. In this variational framework, the solution to the nonlinear optimisation problem is a set of smoothed functions (images) associated with an appropriate Banach space [15] and contours representing discontinuities.

Improvements over Mumford–Shah-based functional are as follows:

(i) In contrast to the Mumford–Shah framework, the investigated functional is able to detect non-closed contours (edges).
(ii) In contrast to Chan–Vese approach, the proposed algorithm here does not fall into local minima in piecewise continuous approximation.
(iii) In contrast to Grayson–Gage–Hamilton-based approaches, the operator-based algorithm proposed here does not suffer from any numerical instability.
(iv) In contrast to Ambrosio–Tortorelli-based approaches, the algorithm proposed here enjoys a robust performance in the presence of excessive noise.

In comparison to *DroG* algorithm, it is demonstrated here that the localisation of the detected edges is improved, with a unique value of the detection performance index for both algorithms. The improvements associated with the geometrical approach over the various segmentation methods mentioned above are indications of the necessity of generalising the work presented in [26]. In comparison to the geometrical method presented in [26] for grey-scale images, two improvements are observed in this paper. First, the algorithm is generalised to the vector-valued images and secondly the underlying operator is derived, and the associated analysis is also presented. In Section 2, the theory is briefly discussed. The implementation method is proposed in Section 3. Numerical results are presented in Section 4, and finally the paper concludes in Section 5. The associated operator with the functional investigated here is analytically derived and compared with the *DroG* operator in the Appendix.

2 Theory

Let us initially consider the scalar-valued image $I(x, y)$ as a piecewise continuous function in which discontinuities are represented as contours. The variational problem, considered for signals [27–29] and images [26], is to find piecewise continuous function $f(x, y)$ whose first and second derivatives are continuous (class C^2) over regions R_i surrounded by a set of contours Γ_i representing discontinuities. This is achieved by minimising

$$E(f,\Gamma)=\frac{1}{2}\sum_i \int\int_{R_i-\Gamma_i} [(f(x,y)-I(x,y))^2+\mu(\nabla f)^2]\,\mathrm{d}x\,\mathrm{d}y \tag{1}$$

In the above functional, the whole image is divided into regions R_i containing objects described by class C^2 functions. Objects are surrounded by contours Γ_i representing discontinuity separating them from their background.

This notion is generalised for vector-valued images $\boldsymbol{I}(x, y)$ with N number of channels corresponding to a location (x, y). For instance, in the case of colour images, $N = 3$ and the channels of the vector image $\boldsymbol{I}(x, y)$ corresponds to RGB values. For vector-valued images, functional (1) is written as

$$E(f,\Gamma)=\frac{1}{2}\sum_{j=1}^{N}\sum_i \int\int_{R_{ij}-\Gamma_{ij}} [(f_j(x,y)-I_j(x,y))^2 + \mu_j(\nabla f_j)^2]\,\mathrm{d}x\,\mathrm{d}y \tag{2}$$

where R_{ij} is a region in R^2 in which $f_j(x, y)$ representing an object in channel j is a continuous function. Similar to functional (1) associated with the grey-scale images, an object in the jth channel is surrounded by discontinuity represented by Γ_{ij}. For the jth channel in region R_{ij}, the minimisation of functional (2) with respect to $f_j(x, y)$, and assuming that contour Γ_{ij} is fixed, leads to the following partial differential equations [26, 27]

$$\mu_j\nabla^2 f_j = f_j - I_j \quad \text{in } R_{ij}-\Gamma_{ij} \tag{3}$$

with the boundary condition

$$\frac{\partial f_j}{\partial n}=0 \quad \text{on } \Gamma_{ij} \tag{4}$$

where μ_j is the smoothing coefficient for channel j.

If Γ_{ij} is varied in a neighbourhood M of a point P on discontinuity as shown in Fig. 1, minimisation of functional (2) is achieved by vanishing the first variation of the functional leading to the following approximation representing the contour equation (see, e.g. [26] for the derivation)

$$(f_j^+(x,y)-I_j(x,y))^2+\mu_j(\nabla f_j^+)^2 - (f_j^-(x,y)-I_j(x,y))^2-\mu_j(\nabla f_j^-)^2=0 \tag{5}$$

where f_j^+ and f_j^- are the variations of $f_j(x, y)$ by varying Γ_{ij} in two different directions to Γ_{ij}^+ and Γ_{ij}^- in a neighbourhood of an arbitrary point. It can be demonstrated that a contour representing discontinuity and therefore satisfying (5) is a minimiser of functional (2) for piecewise continuous low-pass images. It is therefore important to study the second variation of functional (2) with respect to Γ_{ij} the ith contour in channel j. The second variation of functional

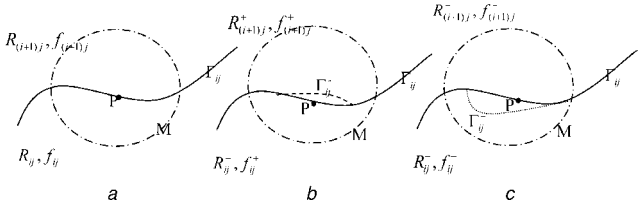

Fig. 1 *Variations of contour Γ_{ij} in a small neighbourhood M (the dashed circle) of a point*

a Contour Γ_{ij} representing discontinuity (edge) separating two regions R_{ij} and $R_{(i+1)j}$
b Γ_{ij} varied to Γ_{ij}^+ separating two regions R_{ij}^+ and $R_{(i+1)j}^+$
c Γ_{ij} varied to Γ_{ij}^- separating two regions R_{ij}^- and $R_{(i+1)j}^-$

(2) with respect to contour Γ_{ij} can be calculated as

$$\delta^2 E = \frac{1}{2}\int\int_M [(f_j^+ - I_j)^2 + \mu_j(\nabla f_j^+)^2]\,dx\,dy + \frac{1}{2}\int\int_M [(f_j^- - I_j)^2 + \mu_j(\nabla f_j^-)^2]\,dx\,dy - \int\int_M [(f_j - I_j)^2 + \mu_j(\nabla f_j)^2]\,dx\,dy \quad (6)$$

where M is the neighbourhood covering the variations of Γ_{ij} and consequently those of $f_j(x, y)$. Using approximation methods, it can be demonstrated that the second variation in (6) is positive for contours representing discontinuities.

If, however, a contour is in a neighbourhood away from any discontinuities where $I_j(x, y)$ is at least of class C^2, we can then write

$$f_j^+(x, y) = f_j^-(x, y) = f_j(x, y)$$
$$\nabla f_j^+ = \nabla f_j^- = \nabla f_j$$

This implies that the second variation for channel j also vanishes. Therefore such contours are saddle points of functional (2). It is hence concluded that contours representing discontinuities are minimisers of functional (2). It should be noted that if such a contour exists only in one of the channels, it would be a minimiser of functional (2) taking care of all channels, although it would be a saddle point in the energy terms associated with other channels.

3 Implementation method

In this section, the geometrical algorithm proposed in [26] is generalised to segment and smooth vector-valued images. Initially, all channels of the original image $\boldsymbol{I}(x, y)$ are linearly smoothed by minimising the linear functional

$$E(f) = \frac{1}{2}\sum_{j=1}^{N}\sum_i \int\int_R [(f_j(x, y) - I_j(x, y))^2 + \mu_j(\nabla f_j)^2]\,dx\,dy \quad (7)$$

By employing Euler–Lagrange equations [30], N partial differential equations are obtained

$$\mu_j \nabla^2 f_j = f_j - I_j, \quad j = 1, 2, \ldots, N \quad (8)$$

A hyper-surface is defined in an $N+2$-dimensional Euclidean manifold [32] as

$$\boldsymbol{S}(x^1, x^2) = x^1\boldsymbol{e}_1 + x^2\boldsymbol{e}_2 + \sum_{j=3}^{N+2} f_{j-2}(x^1, x^2)\boldsymbol{e}_j$$

where (x^1, x^2) are coordinates corresponding to $(x, y) \in R^2$, $\boldsymbol{e}_1, \boldsymbol{e}_2, \ldots, \boldsymbol{e}_{N+2}$ are unit vectors in a Euclidean manifold of $2 + N$ dimensions and $f_1, f_2, \ldots, f_N$ are the solutions of (8).

The metric tensors of this hyper-surface are calculated by generalising the definition of metric tensors for surfaces [31, 32]. As an example, let us consider a colour image in RGB format. The hyper-surface $\boldsymbol{S}$ defined above can therefore be rewritten as

$$\boldsymbol{S}(x, y) = x\boldsymbol{i} + y\boldsymbol{j} + R(x, y)\boldsymbol{r} + G(x, y)\boldsymbol{g} + B(x, y)\boldsymbol{b} \quad (9)$$

where $\boldsymbol{i}, \boldsymbol{j}, \boldsymbol{r}, \boldsymbol{g}$ and $\boldsymbol{b}$ are unit vectors in a five-dimensional Euclidean manifold and $R(x, y)$, $G(x, y)$ and $B(x, y)$ are the smoothed functions for the three channels R, G and B achieved by numerically solving (8) for all three channels.

According to the definition of metric tensors [31, 32]

$$g_{11} = \frac{\partial \boldsymbol{S}}{\partial x}\cdot\frac{\partial \boldsymbol{S}}{\partial x}$$
$$g_{12} = g_{21} = \frac{\partial \boldsymbol{S}}{\partial x}\cdot\frac{\partial \boldsymbol{S}}{\partial y}$$
$$g_{22} = \frac{\partial \boldsymbol{S}}{\partial y}\cdot\frac{\partial \boldsymbol{S}}{\partial y}$$

where

$$\frac{\partial \boldsymbol{S}}{\partial x} = \boldsymbol{i} + \frac{\partial R}{\partial x}\boldsymbol{r} + \frac{\partial G}{\partial x}\boldsymbol{g} + \frac{\partial B}{\partial x}\boldsymbol{b}$$

and

$$\frac{\partial \boldsymbol{S}}{\partial y} = \boldsymbol{j} + \frac{\partial R}{\partial y}\boldsymbol{r} + \frac{\partial G}{\partial y}\boldsymbol{g} + \frac{\partial B}{\partial y}\boldsymbol{b}$$

After some mathematical calculations and noting that the unit vectors $\boldsymbol{i}, \boldsymbol{j}, \boldsymbol{r}, \boldsymbol{g}$ and $\boldsymbol{b}$ are orthogonal to one another, we can write

$$g_{11} = 1 + \left(\frac{\partial R}{\partial x}\right)^2 + \left(\frac{\partial G}{\partial x}\right)^2 + \left(\frac{\partial B}{\partial x}\right)^2$$
$$g_{12} = \left(\frac{\partial R}{\partial x}\right)\left(\frac{\partial R}{\partial y}\right) + \left(\frac{\partial G}{\partial x}\right)\left(\frac{\partial G}{\partial y}\right) + \left(\frac{\partial B}{\partial x}\right)\left(\frac{\partial B}{\partial y}\right)$$
$$g_{22} = 1 + \left(\frac{\partial R}{\partial y}\right)^2 + \left(\frac{\partial G}{\partial y}\right)^2 + \left(\frac{\partial B}{\partial y}\right)^2$$

The discriminant of the metric tensor can therefore be calculated as

$$g = \sqrt{g_{11}g_{22} - g_{12}^2} = \sqrt{\begin{array}{c}(1 + R_x^2 + G_x^2 + B_x^2)(1 + R_y^2 + G_y^2 + B_y^2) \\ -(R_xR_y + G_xG_y + B_xB_y)^2\end{array}}$$

or

$$g = \sqrt{\begin{array}{c}1 + R_x^2 + G_x^2 + B_x^2 + R_y^2 + G_y^2 \\ +B_y^2 + (R_xG_y - G_xR_y)^2 + (R_xB_y - B_xR_y)^2 \\ +(G_xB_y - B_xG_y)^2\end{array}} \quad (10)$$

where $f_x = \partial f/\partial x$ and $f_y = \partial f/\partial y$ in which $f = R$, G or B.

It should be noted that in (10), a discontinuity at a point in an image in either of the channels corresponds to a maximum in g which represents an edge candidate. It is also interesting to note that this is a similar notion to that defined by RMS method proposed in [33], although Sobel and Prewitt operators which are more sensitive in a noisy environment are considered in [33]. In the segmentation step, a zero-crossing in the curvature of the smoothed hyper-surface narrows down the number points for edge point selection among all candidate points in order to choose those points representing discontinuities. The curvature calculation requires computing a normal vector on each point in the hyper-surface. A vector (outer) multiplication should be used to calculate a normal vector at each point [31]. However, vector multiplication is not mathematically defined in Euclidean spaces with more than three dimensions and hence it is not possible to calculate the curvature

of a hyper-surface defined in (9). The numerical experiments in Section 4 will however show that the zero-crossing of the following term occurs in edges in RGB hyper-surfaces.

$$\Re = (R_{xy} + G_{xy} + B_{xy})^2 - (R_{xx} + G_{xx} + B_{xx})(R_{yy} + G_{yy} + B_{yy}) \quad (11)$$

where $f_{xy} = \partial^2 f/\partial x \partial y$, $f_{xx} = \partial^2 f/\partial x^2$ and $f_{yy} = \partial^2 f/\partial y^2$ in which $f = R$, G or B.

We therefore search for zero-crossing of $\Re$ in (11) to select a pixel as an edge candidate.

It is easy to verify that for a single-channel image, the zero-crossing of (11) is reduced to the zero-crossing of the Riemannian curvature [26, 31].

Having calculated the metric tensor and $\Re$ using (10) and (11), the segmentation of vector-valued images is achieved by finding points characterised with maxima in the discriminant of metric tensor computed in (10) and a zero-crossing of $\Re$ defined in (11). The points of the hyper-surface corresponding to points with zero-crossing of $\Re$ associated with the hyper-surface are considered as candidates for edge. The discriminant of the metric tensor calculated in (10) is also examined. If at any point where g is maximised, the value of g is greater than a threshold set by the user to narrow down the candidate points, and the candidate point is characterised with zero-crossing in $\Re$, then it is selected as an edge point. This method is applicable to vector-valued images with more than three channels. It can also be applied to the feature vectors extracted from a texture image by employing a series of filters. This therefore leads to a texture segmentation algorithm.

Having segmented the image, the smoothing process is performed by applying the partial differential equation (3) with the boundary condition (4) on each channel. It should be noted that (3) across edges is not preformed to preserve discontinuities in the smoothed image; instead boundary condition (4) is performed for the optimised solution on edges. In terms of implementation, to find the smoothed image in channel j, the discrete version of (3) is employed to calculate the value of smoothed image at the point (p, q). If the point (p, q) is not selected as an edge point, the smoothed image in channel j is calculated as

$$f_j(p,q) = \frac{\left[\begin{array}{l}\mu(f_j(p-1,q)M(p-1,q)+f_j(p+1,q)M(p+1,q) \\ +f_j(p,q-1)M(p,q-1)+f_j(p,q+1)M(p,q+1))+I_j(p,q)\end{array}\right]}{(M(p-1,q)+M(p+1,q)+M(p,q-1)+M(p,q+1)+1)} \quad (12)$$

where $\boldsymbol{M}$ is a binary mask (matrix) whose elements are zero if a pixel is an edge point, otherwise the elements of $\boldsymbol{M}$ are 1. If however the point (p, q) is on an edge, the corresponding value for the smoothed image at this point is calculated using the boundary condition (4). Equation (4) is a directional derivative along the direction normal to the edge at point (p, q). Therefore it is important to estimate the slope of the tangent to an edge point to be able then to find an estimate for the normal direction. This tangent slope can be estimated in different ways: Either it can be estimated by calculating the partial derivatives of the linearly smoothed image obtained in the segmentation step at the point in question; or in a 3×3 neighbourhood of an edge point, it can be approximately calculated as the slope of the best-fitted line to the detected pixels (in segmentation step) in the neighbourhood. We realise that the latter method to estimate the tangent direction is more robust in the presence of noise. Having calculated the slope of the normal direction to the edge, out of four available directions in this 3×3 neighbourhood, we choose the one which is the closest to the calculated slope. It is then straightforward to find the pixel value of the smoothed image using (4) and the normal direction obtained in the above procedure. For example, if the direction of the contour passing through pixel (p, q) is vertical (parallel to y-axis or the axis representing row p), then the normal direction to the edge is horizontal. Therefore (4) is reduced to $\partial f/\partial x = 0$ at that particular edge point. In discrete domains, this equation can hence be written as either $f(p, q) - f(p, q-1) = 0$ or $f(p, q) - f(p, q+1) = 0$ (q corresponds to x-axis). This is to say that either $f(p, q-1)$ or $f(p, q+1)$ should be chosen to update $f(p, q)$, depending whichever is closer to the pixel value of the original image at (p, q).

It should be noted that the described method to calculate the smoothed image is iterative, so that in each iteration, new pixel values for the smoothed image are calculated until the difference between two smoothed images in two consecutive iterations are less than an error term. It is also noted that in our implementation, we assume $\mu = \mu_j$ for $j = 1, 2, \ldots, N$; however, if different channels are contaminated with different noise levels, different values for μ_j can be set. The proposed algorithm for multi-channel images is presented in Fig. 2.

4 Results

Numerical results of the proposed algorithm are presented in this section; however, it is important to first consider a comparison between the Mumford–Shah functional and functionals (1) and (2). As pointed out in Section 1, a unique solution is not associated with Mumford–Shah

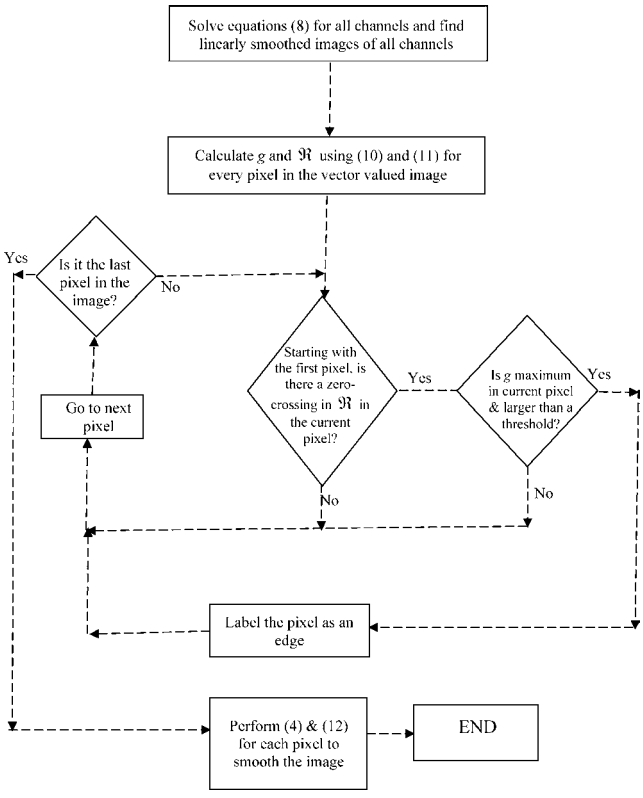

Fig. 2 *Flowchart of the geometrical algorithm*

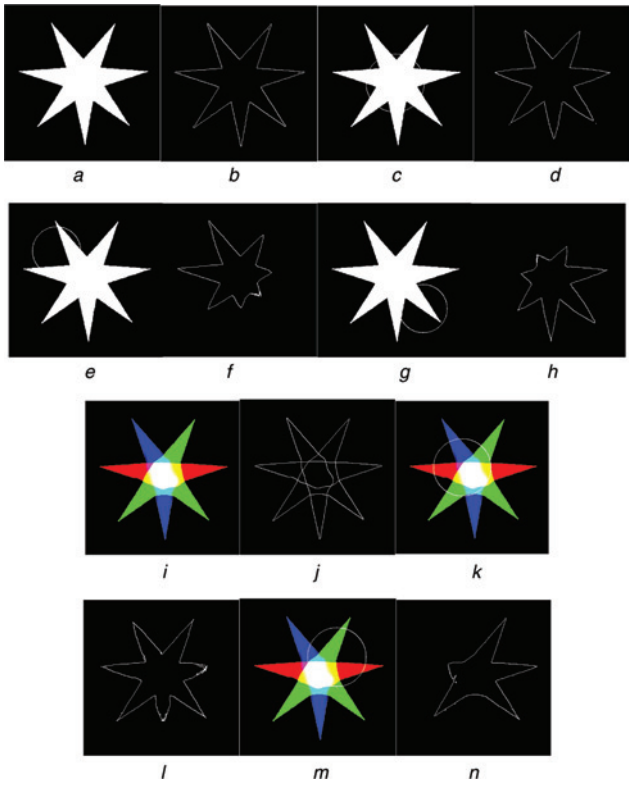

Fig. 3 *Numerical comparison between the functional proposed here and the Mumford–Shah functional*

a An image of a grey-scale star
b Final solution of the functional investigated here
c e and *g* Original image with various initial contours in the implementation of Mumford–Shah functional
d f and *h* Final solutions for Mumford–Shah functional with corresponding initial contours when the coefficient of contour length minimisation term is 100
i An image of coloured star
j Segmented image using the investigated functional
k and *m* Various initial conditions used in Mumford–Shah functional (the coefficient of length minimisation term is set to 10)
l and *n* Final solutions of Mumford–Shah functional with corresponding initial conditions

functional, whereas functionals (1) and (2) are characterised with a unique minimiser. This point is demonstrated in Fig. 3. A contour evolution scheme, based on piecewise constant implementation of Mumford–Shah functional [17], is applied to the star image of Fig. 3*a* with different initial conditions (contours). The initial contours are shown in the figure as circles whose centres are in different locations with respect to the original image. The coefficient of contour minimisation term is set to 100. As shown in the figure, the algorithm implementing Mumford–Shah functional [17] converges to a solution depending on the original location of the initial contour (Fig. 3*c–h*). As the coefficient of the contour minimisation terms approaches zero, all these different solutions converge to a unique solution as expected. On the other hand, the solution of functional (1) is also implemented using the contour evolution framework proposed in [17] with different initial conditions. The algorithm always converges to a unique solution depending on the original image and regardless of the initial contour (Fig. 3*b*). In vector-valued images, it is more obvious that the Mumford–Shah functional is attributed to non-unique solutions. A numerical comparison is also demonstrated in Fig. 3. The contour evolution method for vector-valued images proposed in [20] is applied to the image of Fig. 3*i* with different initial conditions and with the coefficient of contour length minimisation term as low as 10 as shown in Fig. 3*k–n*. The contour evolution algorithm proposed in [20] converges to different solutions depending on the initial condition. Functional (2) is implemented using the contour evolution framework discussed in [20] and applied to the image of Fig. 3*i*. As shown in Fig. 3*j*, functional (2) is always minimised to a unique solution regardless of the initial conditions. This uniqueness of solution of functionals (1) and (2) is essential to formulate an edge (discontinuity) detection operator, and in fact any edge detection algorithm can be regarded as an implementation of functionals (1) and (2) as the aim of any edge detection algorithm is to detect discontinuities. As there is no unique solution to the Mumford–Shah functional, it is not therefore possible to implement it using an operator such as the one proposed in this paper.

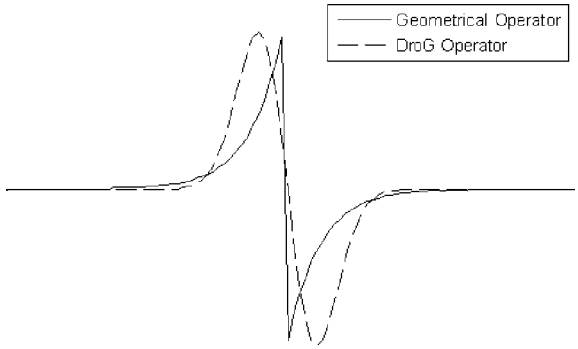

Fig. 4 *Geometrical operator (solid line) calculated in the Appendix with $\mu = 31.83$ (21a) is compared with a DroG operator (21b) with $\sigma = 5$ resulting in the same detection performance ($\Sigma = 5.64$ for both operators, see (23))*

In the Appendix, the impulse response of the 1D geometrical operator is analytically calculated and it is shown in Fig. 4 along with the impulse response of the *DroG* operator with the same detection performance (Σ) for comparison. As can be seen from Fig. 4, there is a sharp transition in the geometrical operator at the centre. This sharp transition produces a delta Dirac function in the localisation term in (22d), and is therefore responsible for a better localisation than that of *DroG* operator.

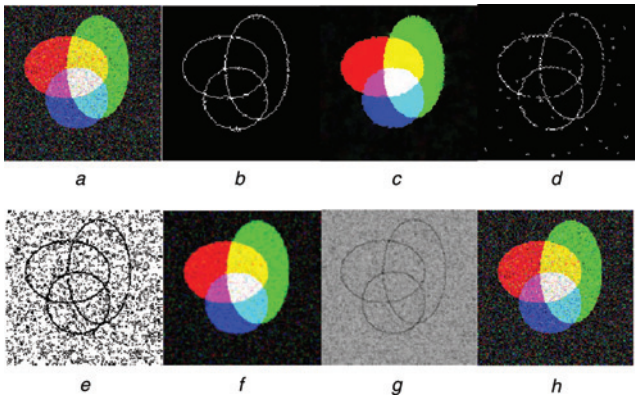

Fig. 5 *Numerical comparison between the geometrical algorithm and the Ambrosio–Torterolli method*

a Noisy image with SNR = 3
b and *c* Segmented and smoothed images using the geometrical algorithm with $\mu = 10$
d Segmented image using the geometrical algorithm with $\mu = 0.01$
e and *f* Segmented and smoothed images of noisy image of *a* using Ambrosio–Torterolli functional with the most empirically optimised parameters
g and *h* Segmented and smoothed images using the G3 approach with the most empirically optimised parameters

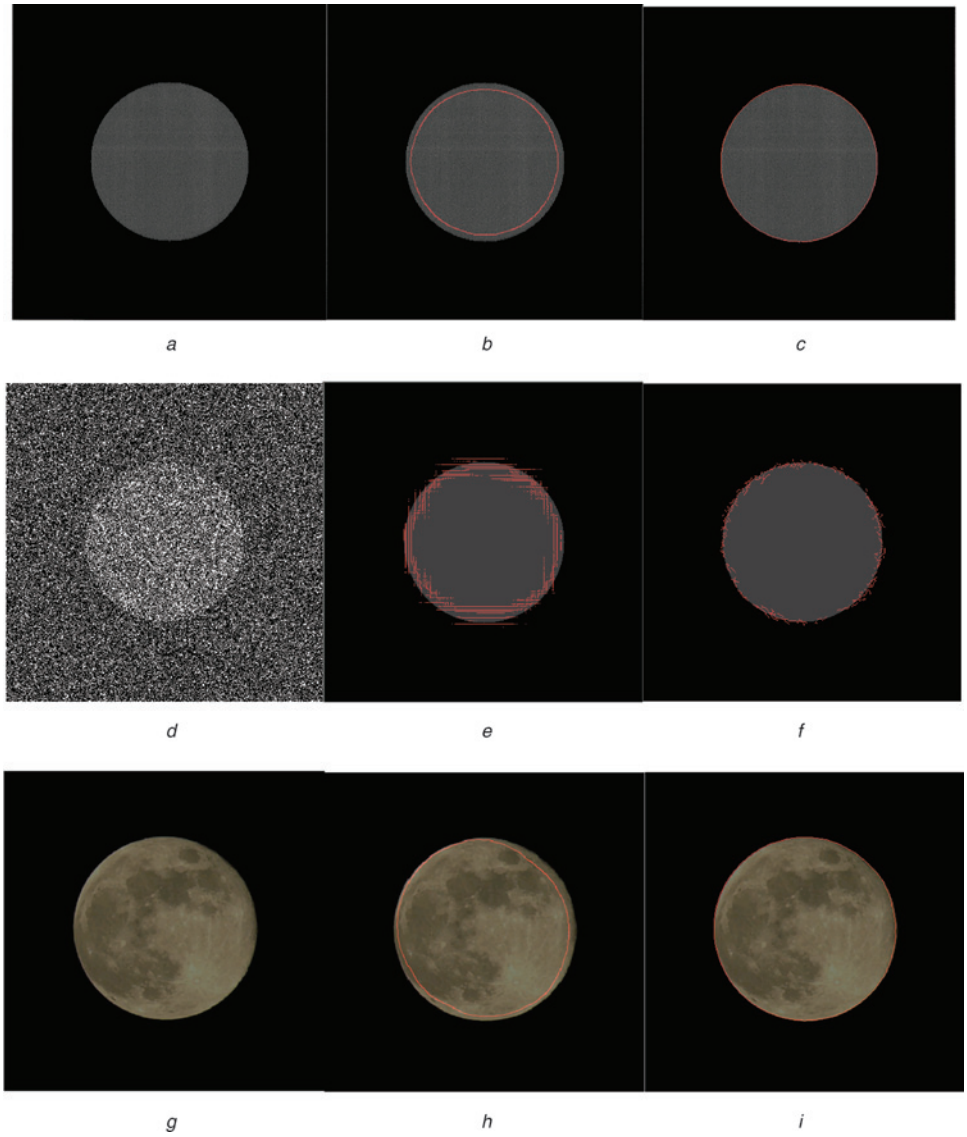

Fig. 6 *Numerical comparison between the proposed algorithm and DroG edge detection algorithm*

a Scanned image
b Segmented image using *DroG*
c Segmented image using geometrical operator
d Noisy image with SNR = 0.04
e Segmented image obtained from *DroG* operator
f Segmental image obtained from the geometrical operator
g Real image of the moon
h Segmented image using *DroG*
i Segmented image using the geometrical operator
$\sigma = 50$ and $\mu = 3183$ are chosen for *DroG* and the geometrical operator, respectively, to result in the equal detection performances in the two operators

The algorithm proposed in Section 3 is applied to the noisy image with SNR = 3 in Fig. 5*a*. The segmented and smoothed images with $\mu = 10$ are shown in Figs. 5*b* and *c*. In the segmentation step, if μ is set to a very small value (e.g. $\mu = 0.01$), then as shown in the figure, some of noise is also segmented. This is because smoothing is not performed properly with a low value for μ. High values of μ result in smoothed images with less fluctuation, therefore leading to improved segmentation. It is noted that the geometrical algorithm with $\mu \geq 1$ results in good smoothing and segmentation effects. In fact, μ values less than 1 lead to operators as wide as almost one pixel. Such operators are sensitive to edges as well as noise resulting in segmented noise being included in edge-detected image. An operator with $\mu = 1$ is as wide as three pixels which is where the smoothing effect begins. The detection performance index or SNR of the operator improves by increasing μ (see 22c), although the algorithm convergence becomes slower.

For comparison, the minimisation of Ambrosio–Torterolli functional that is an asymptotic approximation of the Mumford–Shah functional, using Γ-convergence for vector-valued images [23–25], is applied to the noisy image of Fig. 5*a*. The Ambrosio–Torterolli functional is better behaved than that of Mumford–Shah, but its optimised solution does not lead to an algorithm with a good performance in segmentation and smoothing in the presence of noise. The segmented and restored images are depicted in Fig. 5*e* and *f* with empirically optimised parameters. The G3 approach proposed by Brook *et al.* [23] is also applied to the same noisy image of Fig. 5*a*. The results, based on empirically optimised

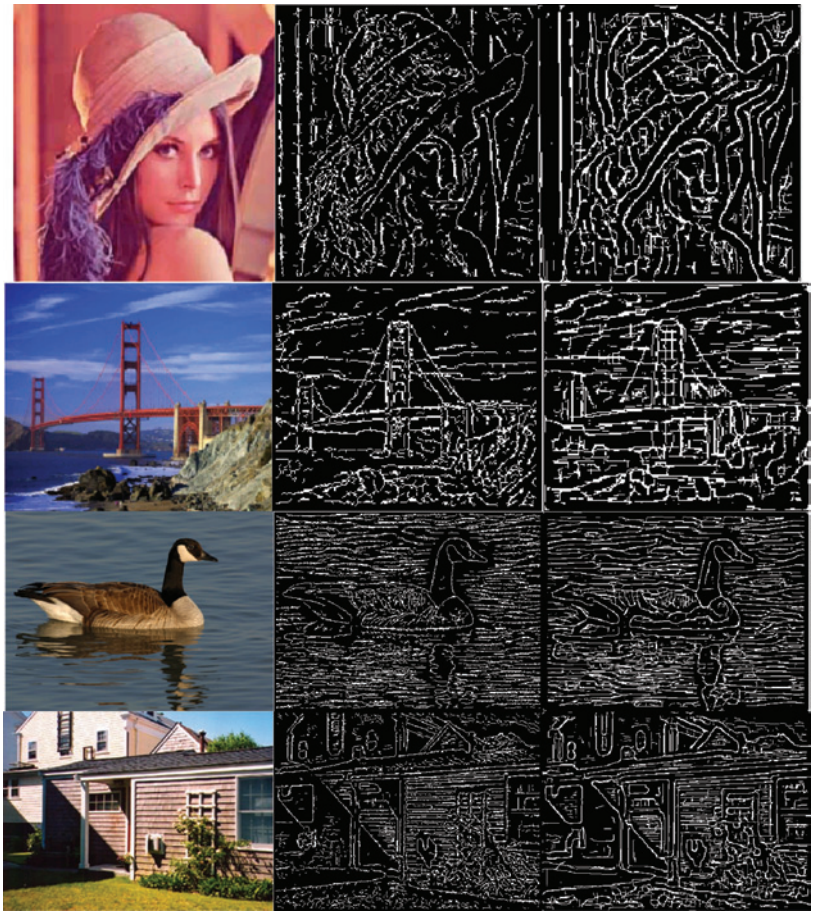

Fig. 7 *Application of geometrical algorithm to colour images for segmentation*

Left column: Various colour images
Middle column: Their segmented images using the geometrical algorithm with $\mu = 31$
Right column: Segmented images using *DroG* operator with $\sigma = 5$

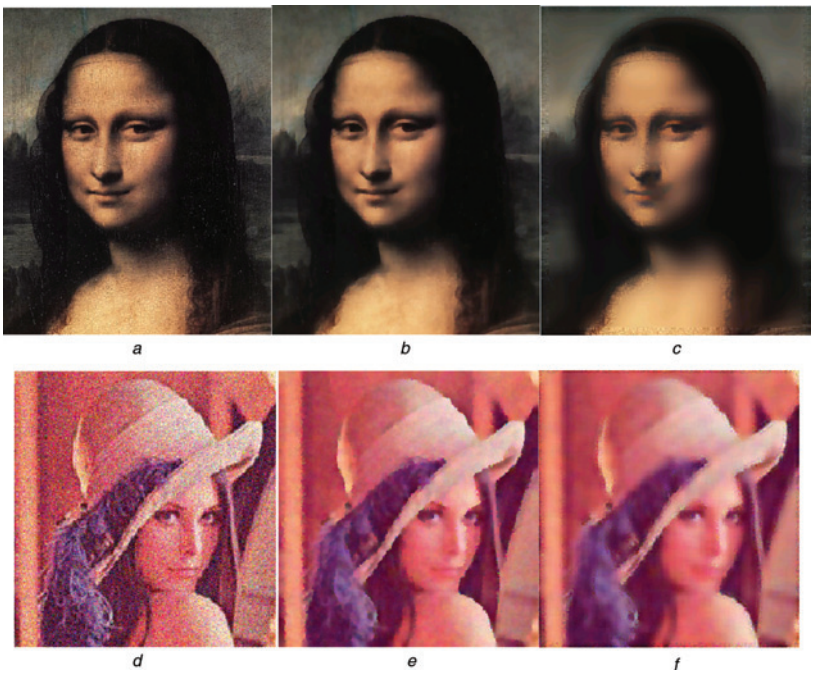

Fig. 8 *Smoothing property of the geometrical algorithm*

a Image of Mona Lisa with some degradation due to its age
b Smoothed image using geometrical approach with $\mu = 10$
c Smoothed image using the Wiener filter
d Noisy Lena image with SNR = 20
e Smoothed image using the geometrical approach with $\mu = 10$
f Smoothed image using the Wiener filter

parameters, are shown in Fig. 5*g* and *h*. As can be seen from Fig. 5*e*–*h*, the methods proposed in [23–25] are very sensitive to noise, that is, they segment the objects as well as some noise. A comparison with Fig. 5*b* and *c* also demonstrates that, in the presence of noise, our restoration method is more robust than that of the methods proposed in [23–25].

The mathematical analysis presented in the Appendix demonstrates that with the equal detection performance for both operators as a criterion, the localisation of the geometrical operator is more accurate than that of the *DroG*. To demonstrate this numerically, two synthetic images and one real image are used as shown in Fig. 6. Fig. 6*a* is obtained by scanning a printed synthetic image (a grey circle in the middle of a dark background) using a scanner with 200 × 200 dpi to simulate an image with real edges. This image is further contaminated with noise as shown in figure 6*d* with $SNR = 0.04$. The *DroG* and the geometrical operator with the same detection performance according to (23), (i.e. $\sigma = 50$ with $3\sigma \times 3\sigma$ window size and $\mu = 3183$) are applied on the images of Figs. 6*a*, 6*d* and 6*g*. The results are shown in the middle and the right columns of fig. 6 as segmented images superimposed on the original images. It can be verified that the considered parameters in both algorithms result in the same detection performance evaluated from equations (22a) and (22c). Since the localisation of the geometrical operator is better than *DroG* with equal Σs (see equations (22a) to (22d)), the edges detected using the geometrical operator is expected to be closer to the real edges of the original images than those detected by *DroG*. This better performance in localisation is observed by comparing the segmentation results obtained by the both algorithms in the middle and right columns of Fig. 6.

The geometrical algorithm is also applied to various coloured images for segmentation as shown in Fig. 7. In this figure, we choose $\mu = 31$ for all channels. *DroG* with $\sigma = 5$, resulting in the same detection performance index as that of the geometrical algorithm, is also applied to the colour images of Fig. 7, as depicted in the right column of Fig. 7. It is interesting to note that although some parts of images with finer details are segmented by the geometrical approach, *DroG* algorithm either fails to detect or distorts the edges associated with some of these fine details. This is particularly observed in the hat furs of Lena (the first row), the rocks in Golden Gate (the second row), the Duck feathers (the third row) and bushes in the house image (the fourth row). These effects in *DroG* approach worsened by increasing the standard deviation of the Gaussian operator σ, are attributed to two factors: (i) the shifting away phenomenon of edges in *DroG* discussed in Fig. 6, and (ii) the average distance between the zero-crossings of the convolved image, which is initially contaminated with random noise, is proportional to σ, the standard deviation of *DroG*, as demonstrated in [34–36]. Some of the finer details in the above images are therefore removed in the same way as is the random noise.

The smoothing property of the proposed algorithm in this paper is employed to reconstruct the Mona Lisa image (Fig. 8*b*) without compromising the edges of the original image (i.e. prior to degradation through time as evident in Fig. 8*a*). This smoothing property of the geometrical algorithm is absent in a standard edge detection algorithm such as *DroG*. For comparison, the Wiener filter is also applied to the Mona Lisa image to remove the effects of degradation as shown in Fig. 8*c*. It is obvious from Fig. 8*b* and *c* that the smoothing method proposed here preserves the discontinuities; whereas the Wiener filter smoothes both degradations and discontinuities to result in the image of Fig. 8*c* with blurred edges. The image of Lena is also contaminated with zero mean Gaussian noise to result in the noisy image of Fig. 8*d* with SNR = 20. The geometrical algorithm with $\mu = 10$ and the Wiener filter are applied to the image of Fig. 8*d*, the results being depicted in Fig. 8*e* and *f*, respectively. It is again observed that the geometrical approach proposed here smoothes the image while preserving the edges, whereas the smoothed image obtained by applying the Wiener filter has blurred edges. It is noted that smoothing of the geometrical algorithm deteriorates as SNRs becomes low. This is because of the fact that with higher levels of noise, higher values for μ are required. As the value of μ increases, the smoothed image approaches the piecewise constant approximation suppressing both noise and low-frequency contents of the image. If lower values for μ is chosen to keep the low-frequency contents of the image, then some noise is also allowed to remain on the smoothed image. As a matter for future study, the smoothing process for low SNR images therefore requires three fundamental improvements. First, smoothing should be performed locally rather than globally on regions where there is no discontinuity. Secondly, in a local neighbourhood, the best-fit surface (for images) and function (for signals) should be calculated for the available pixels in that neighbourhood. Thirdly, nurbs and splines can then be used for more smoothing effects.

The proposed method in this paper is, however, more expensive than *DroG* edge detector. For example, for an image with the resolution 100 × 100, the CPU time of a PC workstation with 2.5 GHz CPU clock for the geometrical algorithm and the *DroG* edge detector are 2.84 and 0.11 s, respectively.

5 Conclusion

A variational method is considered in this paper for segmentation and smoothing of vector-valued images to mathematically model edge detection in colour images. It is demonstrated in this paper that the investigated functional has a unique solution in contrast with Mumford–Shah functional.

As a result of this unique solution, an edge-based algorithm using geometrical properties such as metric tensor of a hyper-surface containing smoothed surfaces is proposed for implementation by introducing a linear operator. This operator is characterised with a better localisation property than that of the *DroG* operator, although the geometrical algorithm proposed here is numerically more expensive. It is demonstrated in this paper that the improved localisation of the geometrical operator is attributed to a sharp transition at the centre of the operator. For the future work, this notion therefore introduces a new possibility of investigating a set of operators whose centre is characterised with a sharp transition and are as fast as the *DroG* operator. A comparison between the geometrical method and other traditional methods in the literature presented here shows that the proposed method is robust in a noisy environment. In addition to 2D vector-valued images, the geometrical algorithm can also be generically used in the segmentation and restoration of 1D signals. As a future project, the smoothing for low SNR images can also be improved by minimising the functional locally to find the best-fit surfaces based on nurbs and splines. The other interesting future work is to modify the functional for volumetric 3D images which is a well-known challenge in the Mumford–Shah framework.

6 Acknowledgments

The authors thank Prof. D. Mumford for his useful advice, Prof. M. Hammerton for his proof-reading and the

anonymous reviewers for their constructive and interesting comments.

7 References

1 Tikhonov, A.N., and Arsenin, V.Y.: 'Solutions of ill-posed problems' (Winston & Sons, Washington, DC, 1977)
2 Rudin, L.I., Osher, S., and Fatemi, E.: 'Nonlinear total variation based noise removal algorithms', *Physica D*, 1992, **60**, pp. 259–268
3 Blomgren, P., and Chan, T.F.: 'Color TV: total variation methods for restoration of vector valued images', *IEEE Trans. Image Process.*, 1998, **7**, (3), pp. 304–309
4 Kass, M., Witkin, A., and Terzopoulos, D.: 'Snakes: active contour models', *Int. J. Comput. Vis.*, 1987, **1**, pp. 321–331
5 Cohen, L.D.: 'On active contour models and balloons', *CVGIP, Image Underst.*, 1991, **53**, (2), pp. 211–218
6 Aubert, G., and Kornprobst, P.: 'Mathematical problems in image processing: partial differential equations and calculus of variations' (Springer-Verlag, New York, 2002)
7 Sethian, J.A.: 'Level set methods: evolving interfaces in geometry, fluid mechanics, computer vision and material science' (Cambridge University Press, 1996)
8 Osher, S., and Sethian, J.: 'Fronts propagating with curvature-dependent speed: algorithms based on Hamilton–Jacobi formulations', *J. Comput. Phys.*, 1988, **79**, pp. 12–49
9 Morel, J.L., and Solimini, S.: 'Variational methods in image segmentation' (Birkhauser, Boston, 1995)
10 Caselles, V., Kimmel, R., and Sapiro, G.: 'Geodesic active contours'. Proc. 5th Int. Conf. on Computer Vision, IEEE Computer Society Press, 1995, pp. 694–699
11 Caselles, V., Kimmel, R., and Sapiro, G.: 'Geodesic active contours', *Int. J. Comput. Vis.*, 1997, **22**, (1), pp. 61–79
12 Sapiro, G., and Ringach, D.L.: 'Anisotropic diffusion of multi-valued images with applications to color filtering', *IEEE Trans. Image Process.*, 1996, **5**, pp. 1582–1586
13 Sapiro, G.: 'Color snakes', *Comput. Vis. Image Underst.*, 1997, **68**, (2), pp. 247–253
14 Mumford, D., and Shah, J.: 'Optimal approximations by piecewise smooth functions and associated variational problems', *Comm. Pure Appl. Math.*, 1989, **42**, (4), pp. 577–688
15 Kreyzig, E.: 'Introductory functional analysis with applications' (John Wiley & Sons, 1989)
16 Tsai, A., Yezzi, A., and Willsky, A.S.: 'Curve evolution implementation of the Mumford–Shah functional for image segmentation, denoising, interpolation and magnification', *IEEE Trans. Image Process.*, 2001, **10**, (8), pp. 1169–1186
17 Chan, T.F., and Vese, L.A.: 'Active contours without edges', *IEEE Trans. Image Process.*, 2001, **10**, (2), pp. 266–277
18 Hintermuller, M., and Ring, W.: 'An inexact-CG-type active contour approach for the minimization of the Mumford–Shah functional', *J. Math. Imaging Vis.*, 2004, **20**, pp. 19–42
19 Vese, L.A., and Chan, T.F.: 'A multiphase level set framework for image segmentation using the Mumford and Shah model', *Int. J. Comput. Vis.*, 2002, **50**, (3), pp. 271–293
20 Chan, T.F., Sandberg, B.Y., and Vese, L.A.: 'Active contours without edges for vector-valued images', *J. Vis. Commun. Image Represent.*, 2000, **11**, pp. 130–141
21 Chan, T.F., and Vese, L.A.: 'Level set algorithm for minimising the Mumford–Shah functional in image processing'. Proc. IEEE Workshop on Variational and Level Set Methods in Computer Vis., 2001, pp. 161–168
22 Vese, L.A.: 'Multiphase object detection and image segmentation', in Osher, S., and Paragios, N. (Eds.): 'Geometrical level set methods in imaging, vision, and graphics' (Springer Verlag, 2003), pp. 175–194
23 Brook, A., Kimmel, R., and Sochen, N.A.: 'Variational restoration and edge detection for color images', *J. Math. Imaging Vis.*, 2003, **18**, pp. 247–268
24 Ambrosio, L., and Tortorelli, V.M.: 'Approximation of functionals depending on jumps by elliptic functionals via Γ-convergence', *Comm. Pure Appl. Math.*, 1990, **43**, (8), pp. 999–1036
25 Ambrosio, L., and Tortorelli, V.M.: 'On the approximation of free discontinuity problems', *Boll. Un. Mat. Ital. B(7)*, 1992, **6**, (1), pp. 105–123
26 Mahmoodi, S., and Sharif, B.S.: 'Nonlinear optimisation method for image segmentation and noise reduction using geometrical intrinsic properties', *Image Vis. Comput.*, 2006, **24**, pp. 202–209
27 Mahmoodi, S., and Sharif, B.S.: 'Noise reduction, smoothing and time interval segmentation of noisy signals using an energy optimisation method', *IEE Proc., Vis., Image Signal Process.*, 2006, **153**, (2), pp. 101–108
28 Mahmoodi, S., and Sharif, B.S.: 'Signal segmentation and denoising algorithm based on energy optimisation', *Signal Process.*, 2005, **85**, (9), pp. 1845–1851
29 Mahmoodi, S., and Sharif, B.S.: 'A nonlinear variational method for signal segmentation and reconstruction using level set method', *Signal Process.*, 2006, **86**, pp. 3496–3504
30 Manderscheid, U.B.: 'Introduction to the calculus of variations' (Chapman & Hall, 1991)
31 Lipschutz, M.M.: 'Theory and problems of differential geometry'. Schaum's Outline Series, (McGraw-Hill Book Company, 1969)
32 Kay, D.C.: 'Tensor calculus'. Schaum's Outline Series, (McGraw-Hill Book Company, 1988)
33 Di Zenzo, S.: 'A note on the gradient of a multi-image', *Comput. Vis. Graph. Image Process.*, 1986, **33**, pp. 116–125
34 Canny, J.: 'Finding edges and lines in images'. MIT Artificial Intelligence Laboratory Report, Technical Report 720, 1983
35 Rice, S.O.: 'Mathematical analysis of random noise', *Bell Syst. Tech. J.*, 1945, **24**, pp. 46–156
36 Canny, J.: 'A computational approach to edge detection', *IEEE Trans. Pattern Anal. Mach. Intell.*, 1996, **8**, (6), pp. 679–698
37 Kreyzig, E.: 'Advanced engineering mathematics' (John Wiley & Sons, 2006)

8 Appendix

In this section, the proposed geometrical algorithm is theoretically evaluated using the mathematical criteria such as detection performance and localisation indices considered by Canny [34, 36]. Before evaluating these criteria, we need to calculate the impulse response of the edge detector operator described in the text. We follow the tradition employed in [34, 36] to use one-dimensional signals for analytical comparisons. For 1D signals, the Helmholtz-type differential equation [37] minimising the 1D functional [27, 28] is reduced to

$$\mu \frac{\mathrm{d}^2 f}{\mathrm{d}x^2} = f - g \tag{13}$$

where f is the smoothed signal and g the original signal. Let us first calculate the step response of the system defined by (13). The impulse response of the edge detector can then be calculated using this step response. Let us therefore assume that $g(x)$ is defined as

$$g(x) = H(x) = \begin{cases} 1, & x > 0 \\ 0, & x < 0 \end{cases} \tag{14}$$

where $H(x)$ is the Heaviside (step) function [37]. As f is of class C^2, we expect f and its first derivative to be continuous at $x = 0$ and that the following boundary conditions for the step response are met

$$\lim_{x \to +\infty} f(x) = 1 \tag{15a}$$

$$\lim_{x \to -\infty} f(x) = 0 \tag{15b}$$

It is straightforward to see that the general solution to the differential equation (13) with input (14) is

$$f(x) = \begin{cases} A\,\mathrm{e}^{-x/\sqrt{\mu}} + B\,\mathrm{e}^{x/\sqrt{\mu}} + 1, & x > 0 \\ C\,\mathrm{e}^{x/\sqrt{\mu}} + D\,\mathrm{e}^{-x/\sqrt{\mu}}, & x < 0 \end{cases} \tag{16}$$

The boundary conditions (15a) and (15b) require that

$$B = 0$$

$$D = 0$$

Since f and its first derivative are continuous at $x = 0$, then

$$f(0^-) = f(0^+) \tag{17a}$$

$$\frac{\mathrm{d}f}{\mathrm{d}x}(0^-) = \frac{\mathrm{d}f}{\mathrm{d}x}(0^+) \tag{17b}$$

By applying conditions (17a) and (17b) to function f in (16), the following linear system for A and C, are obtained

$$C = A + 1$$
$$C = -A$$

Therefore

$$A = -\frac{1}{2}$$
$$C = \frac{1}{2}$$

The step response f of the system characterised by (13) can therefore be written as

$$f(x) = \begin{cases} 1 - \frac{1}{2}e^{-x/\sqrt{\mu}}, & x > 0 \\ \frac{1}{2}e^{x/\sqrt{\mu}}, & x < 0 \end{cases} \tag{18}$$

If the impulse response of the system with (13) is represented by $J(x)$, then $f(x)$ can be written as

$$f(x) = J(x) * H(x)$$

where $H(x)$ is Heaviside (step) function and $*$ represents convolution operation. To find the edge location, the first derivative of the function in (18) is examined, that is, $f'(x)$ in the following equation is examined

$$f'(x) = J'(x) * H(x) \tag{19}$$

The function $f'(x)$ and $J'(x)$ are therefore step response and impulse response of the edge detector operator, respectively. To calculate the impulse response of the edge detector operator $J'(x)$ analytically, we take one more derivative on both sides of (19)

$$f''(x) = J'(x) * H'(x) = J'(x) * \delta(x) = J'(x) \tag{20}$$

Therefore the impulse response of the edge detector operator is the second derivate of function f. Using (18) and (20), the impulse response of the edge detector $h(x)$ can be calculated as

$$J'(x) = f''(x) = h(x) = \begin{cases} \frac{-1}{2\mu}e^{-x/\sqrt{\mu}}, & x > 0 \\ \frac{1}{2\mu}e^{x/\sqrt{\mu}}, & x < 0 \end{cases} \tag{21a}$$

The impulse response for a derivative of Gaussian filter (*DroG*) is [36]

$$h(x) = -\frac{x}{\sigma^2}e^{-x^2/2\sigma^2} \tag{21b}$$

For illustration and comparison purposes, the impulse responses (operators) of the geometrical approach (21a) and *DroG* (21b) are depicted in Fig. 4.

Let us now evaluate localisation and detection performance terms considered by Canny in [34, 36] for both impulse responses given in (21a) and (21b). For the *DroG* filter, the detection performance and localisation terms are calculated as [36]

$$\text{Detection performance} = \Sigma(h) = \frac{\left|\int_{-\infty}^{0} h(x)\,dx\right|^2}{\int_{-\infty}^{+\infty} h^2(x)\,dx} = \frac{2\sigma}{\sqrt{\pi}} \tag{22a}$$

$$\text{Localisation} = \Lambda(h') = \frac{|h'(0)|^2}{\int_{-\infty}^{+\infty} h'^2(x)\,dx} = (1/\sigma^2)^2/3\sqrt{\pi}/4\sigma^3 = 4/(3\sigma\sqrt{\pi}) \tag{22b}$$

For the geometrical operator calculated in (21a), the above two terms are computed as

$$\Sigma = \sqrt{\mu} \tag{22c}$$

$$\Lambda = \frac{(1/\mu^2)(\delta(0))^2}{1/8\mu^2\sqrt{\mu} + 1/2\mu^2\delta(0)} \simeq 2\delta(0) \tag{22d}$$

where $\delta(x)$ is the Dirac delta function. It is noted that in the calculations involved in the estimation of the localisation, Dirac function is approximated as

$$\delta(x) = \lim_{\varepsilon \to 0} \frac{\varepsilon}{\pi(x^2 + \varepsilon^2)}$$

It is interesting to note that for a given detection performance (Σ) for both operators, the localisation of the geometrical operator is higher (see (22a)–(22d)). If (22a) and (22c) are set equal, then μ and σ for the given detection performance become related as

$$\sigma = \frac{\sqrt{\pi\mu}}{2} \tag{23}$$

Therefore parameter σ can be calculated for a given μ and vice versa. Given the parameters μ and σ related with (23), the localisation of geometrical operator is better, as it is equal to the Dirac function. It is noted that in digital signals and images, the Dirac function is limited to the resolution of digitisation. This higher localisation property associated with the geometrical operator is numerically demonstrated in the text with some examples in Fig. 6.